

Article

Solderability, Microstructure, and Thermal Characteristics of Sn-0.7Cu Alloy Processed by High-Energy Ball Milling

Ashutosh Sharma ¹, Min Chul Oh ^{1,2}, Myoung Jin Chae ¹, Hyungtak Seo ^{1,*}
and Byungmin Ahn ^{1,*}

¹ Department of Energy Systems Research and Department of Materials Science and Engineering, Ajou University, Suwon 16499, Korea; ashu@ajou.ac.kr (A.S.); minlovehyo@ajou.ac.kr (M.C.O.); whe668@ajou.ac.kr (M.J.C.)

² Metals Forming Technology R&D Group, Korea Institute of Industrial Technology, Incheon 21999, Korea

* Correspondence: hseo@ajou.ac.kr (H.S.); byungmin@ajou.ac.kr (B.A.); Tel.: +82-31-219-3532 (H.S.); +82-31-219-3531 (B.A.); Fax: +82-31-219-1613 (B.A.)

Received: 16 February 2020; Accepted: 10 March 2020; Published: 13 March 2020



Abstract: In this work, we have investigated the role of high-energy ball milling (HEBM) on the evolution of microstructure, thermal, and wetting properties of an Sn-0.7Cu alloy. We ball-milled the constituent Sn and Cu powders in eutectic composition for 45 h. The microstructural studies were carried out using optical and scanning electron microscopy. The melting behavior of the powder was examined using differential scanning calorimetry (DSC). We observed a considerable depression in the melting point of the Sn-0.7Cu alloy (≈ 7 °C) as compared to standard cast Sn-0.7Cu alloys. The resultant crystallite size and lattice strain of the ball-milled Sn-0.7Cu alloy were 76 nm and 1.87%, respectively. The solderability of the Sn-0.7Cu alloy was also improved with the milling time, due to the basic processes occurring during the HEBM.

Keywords: high-energy ball milling; soldering; joining; microstructure; interface

1. Introduction

Conventional Pb-bearing solders (Sn-37Pb, and Sn-40Pb) have been used extensively in electronic interconnects and microelectronic packaging devices for decades. The popularity of Pb-bearing solders is mainly due to its low cost and attractive properties required for soldering, e.g., low melting point, excellent wetting, and the absence of undesirable reaction compounds [1,2]. However, there are various regulations over the usage of Pb-bearing solder alloys due to their inherent toxicity to the human environment [3,4].

The last few decades have witnessed numerous research activities to find a substitute for Pb-bearing solders. Various Pb-free solders have been developed that are binary, ternary, or multicomponent alloys based primarily on Sn [5,6]. The most popular Pb-free solder is based on a ternary Sn-Ag-Cu (SAC) alloy [7]. SAC alloys have served in microelectronic packaging industries as a potential alternative to Sn-Pb alloys. However, there are still a few technology-related issues to consider when using SAC alloys [8]. The major concern in the use of Ag-bearing solder alloys is their higher melting point compared to Sn-Pb solders [9]. Another drawback is the high price of Ag across the globe. In addition, the reliability of Pb-free solders to various metallic substrates is still a big challenge. The presence of brittle Ag₃Sn intermetallic compounds (IMCs) in solders containing Ag deteriorates the joint properties [10]. Moreover, these popular SAC alloys, used in electronic packaging, contain additional Cu₆Sn₅, Cu₃Sn, etc., IMCs [8–10]. Other important Pb-free alloys include components like Cu, Bi, Zn, In, and Sb. Some of these have shown promising results, like lower melting points

than Sn-Pb; however, the inherent brittleness of Bi, the scarcity of In in the earth's crust, the mild toxicity of Sb, and the oxidation issues associated with Zn have prevented their application [7,8,11–16]. Among these binary alloys, the Sn-Cu alloy seems to be a great candidate because of its cheaper price, absence of harmful Ag₃Sn IMCs, and good wetting. The eutectic Sn-0.7Cu alloy is widely used in wave soldering; however, it is not usually used in reflow soldering due to its poor strength and higher melting point than SAC alloys [17,18].

Therefore, melting point depression is of utmost importance in electronics packaging. Low-melting-point solder alloys may ease wetting to common metal substrates in electronic applications [19]. It is also established that grain size refinement allows for a possible depression in melting temperature. The grain boundary's excess energy acts as a driving force that causes a decrease in the enthalpy of melting. A disordered interface is believed to promote a depression in melting enthalpy. Thus, microstructural modification of solder alloys at nanoscale represents a good option for tailoring the melting point, in addition to mechanical strength [20–22]. Other methods include the use of alloying, or the addition of nanoparticles inside the soft metal matrix to enhance the melting point depression [23–25]. However, the use of secondary reinforcements has shown segregation and issues of poor wetting [24,25].

Common methods of alloy fabrication include sol-gel, chemical methods, vapor deposition techniques, melting and casting, severe plastic deformation, and high-energy ball milling (HEBM). Among these, HEBM has emerged as one of the exciting methods for the development of advanced nanostructured alloys [26]. HEBM is a potential method to produce low-melting-point nanocrystalline materials through continuous nanostructuring of metal powders. In addition, the high fraction of grain boundaries obtained during the milling process can also strengthen the mechanical and joint properties of materials when reflowed at higher temperatures [26–28].

There are various reports on the development of Pb-free solders via HEBM. Huang and his co-workers mechanically alloyed Sn-Zn and Sn-Sb alloy by HEBM [29]. Lai et al. produced Sn-Ag and Sn-Ag-Bi alloys by HEBM. They also obtained an enhancement of the wetting and soldering properties of these alloys [30]. Other researchers have fabricated Pb-free solders with several ceramic nano-reinforcements, e.g., ZrO₂, Al₂O₃, SiC, SnO₂, TiO₂, CNT, and graphene, through HEBM [24,25,31–35]. The present literature provides limited information on the lowering of the melting point of the existing Sn-0.7Cu alloy and the improvement of its mechanical strength.

Inspired by the aforementioned discussion, we have attempted to address the above-mentioned literature gaps. We fabricated an Sn-0.7Cu alloy by HEBM for 45 h. The melting properties of Sn-0.7Cu were evaluated after the milling. To assess the wetting properties of the Sn-0.7Cu alloy, the spreading behavior of the milled Sn-0.7Cu powders on copper substrates was also calculated.

2. Materials and Methods

The materials used for the HEBM were Sn and Cu powder (99.95% purity, Loba Chemie, Bangalore, India). The HEBM was performed at 300 rpm for 45 h in tungsten carbide (WC) vials containing 50 WC balls. The ball to powder weight ratio was 10:1. Stearic acid (0.2 wt. %) was mixed with the powder to avoid cold welding of the powder particles during the HEBM process. Table 1 shows the composition of the Sn-0.7Cu alloy milled for 45 h.

Table 1. Selected composition of the Sn-Cu alloy.

Element	Composition (wt. %)	
	Cu	Sn
Values	0.7	99.3

The Sn-0.7Cu powder was characterized by X-ray diffraction (XRD, Rigaku, Miniflex, Rigaku Corporation, Tokyo, Japan) to investigate the phase and structural evolution during the HEBM. The samples

were prepared by mounting powder on glass holder slides with dimensions of 10 mm × 10 mm × 2 mm. The XRD was done at operating parameters of 35 kV and 35 mA with Cu K_α radiation (λ = 1.54056 Å). The samples were scanned from 25° to 70°. The crystallite size and lattice strain induced in the powder particles during HEBM were calculated using the Williamson-Hall (W-H) equation method [36].

The microstructural studies were done by scanning electron microscopy (SEM, Hitachi-4800, Tokyo, Japan). Prior to the SEM studies, the samples were handled and kept inside a glove box filled with Ar gas. The composition of the powder was identified using energy-dispersive X-ray spectroscopy (EDS, INCA, Oxford Instruments, Oxfordshire, UK).

To further study the alloying process, powder samples milled for various times were compacted into small pellets (Φ = 4mm) at 250 Pa [37]. The compacted samples were then mounted and tested for microhardness after metallographic polishing of up to 1 μm. The microhardness tests were performed by Vickers microhardness tester (Mitutoyo HM 200 series, Mitutoyo Corporation, Kanagawa, Japan) at 25 gf and 20 s. The microhardness measurements were repeated five times, and the average value was reported.

The melting point of the milled powders for various times was measured using a DSC (Diamond DSC, Perkin-Elmer, Waltham, MA, USA). The analysis was done from 50–350 °C at a heating rate of 10 °C/min. The samples were heated in an alumina pan under N₂ atmosphere. Assuming no weight gain or loss during heating, the enthalpy of melting (in J/g) was calculated by area under the curve divided by the sample's weight.

The wetting of the HEBM-ed Sn-0.7Cu powder samples was determined by the spread ratio method. The powder samples were reflowed at 250 °C on copper substrates. The change in the area spread ratio before and after melting was calculated.

3. Results and Discussion

The structural characterization of the phases evolved after milling the Sn-0.7Cu powder for 45 h, as shown in Figure 1.

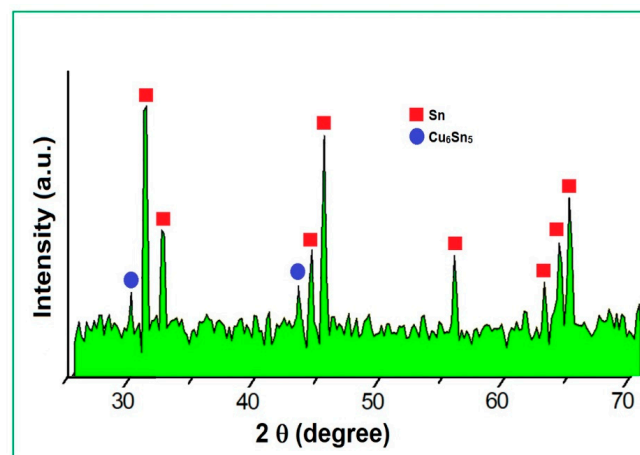


Figure 1. XRD pattern of the Sn-0.7 wt. % Cu powder after milling for 45 h.

The XRD diagram indicated the presence of tetragonal β-Sn. A few instances of Cu₆Sn₅ IMCs were also observed due to the diffusion of Cu atoms across the grain boundary. We also calculated the crystallite size and lattice strain of the Sn-0.7Cu alloy using the W-H equation (Table 2). According to the W-H equation [36], the peak broadening is related to the crystallite size (*D*), lattice strain (*ε*), full width at half maximum (*β*_{hkl}), and Bragg angle (*θ*) by

$$\beta_{hkl} \cos \theta = \frac{K\lambda}{D} + 4\varepsilon \sin \theta \quad (1)$$

where $K = 0.9$; the shape factor (assuming Cauchy—distribution), and the wavelength of the X-rays, $\lambda = 1.5406 \text{ \AA}$. After subtracting the instrumental broadening, the resultant peak broadening is related to $\beta_{\text{hkl}}^2 = \beta_{\text{measured}}^2 - \beta_{\text{instrument}}^2$. The instrumental broadening correction was done by using a reference standard strain-free sample. The sample was obtained by annealing the same powder at $900 \text{ }^\circ\text{C}$.

Table 2 shows that the crystallite size of the β -Sn phase was reduced continuously with milling time. The final crystallite size after 45 h milling was 76 nm. The lattice strain also increased with milling time and approached a value of 1.87% after 45 h.

Table 2. Crystallite size and lattice strain.

Milling Time (h)	Crystallite Size (D, nm)	Lattice Strain (%)
5	185 ± 14	0.23 ± 0.07
15	173 ± 12	0.39 ± 0.08
25	159 ± 11	0.42 ± 0.09
35	139 ± 09	0.51 ± 0.11
45	76 ± 05	1.87 ± 0.24

The crystallite size refinement was attributed to the continuous fracturing and welding of powder particles together at the initial stages of HEBM, followed by the work hardening of powder particles [36–38]. The nanostructuring was also associated with the introduction of lattice strains due to the continuous deformation of the powder particles [26–28].

The SEM images of the Sn-0.7Cu powder after undergoing the HEBM process for various milling times are shown in Figure 2.

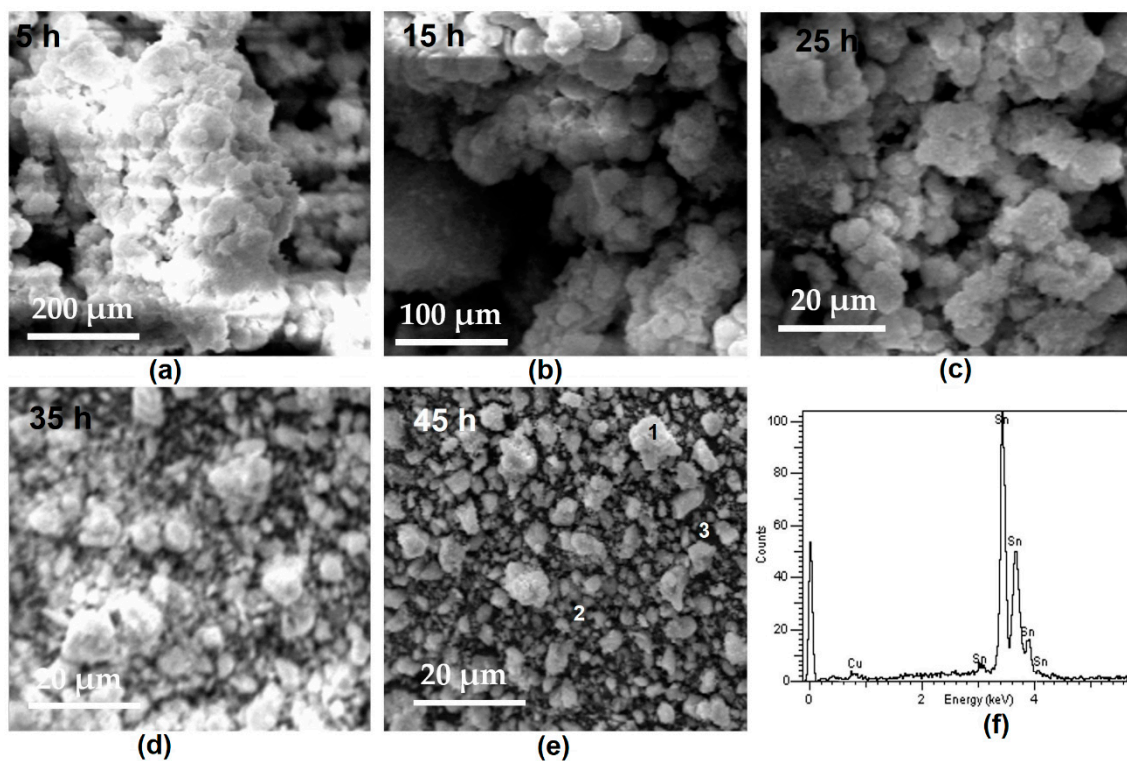


Figure 2. SEM micrograph of Sn-0.7Cu alloy milled for various times. (a) 5 h, (b) 15 h, (c) 25 h, (d) 35 h, (e) 45 h, and (f) energy-dispersive X-ray spectroscopy (EDS) analysis.

The compositional analysis was performed using the EDS analysis (Table 3). The presence of the β -Sn and Cu_6Sn_5 IMCs were noticed from Table 3 without any other impurity elements.

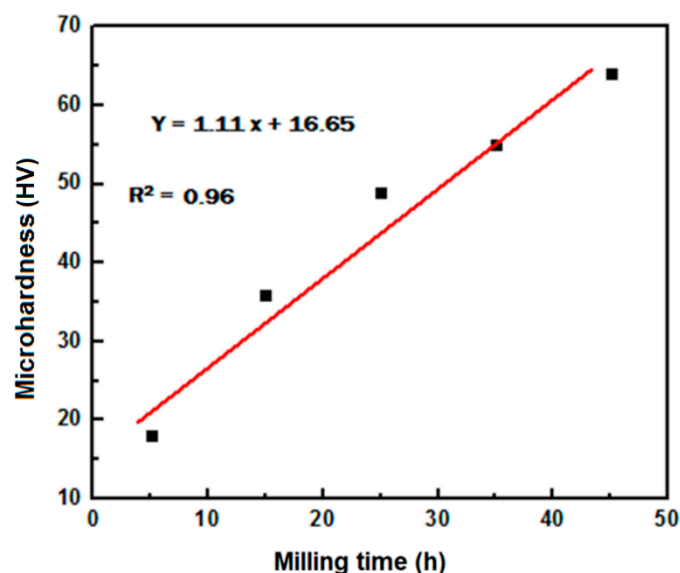
Table 3. Compositional analysis of Sn-0.7 wt. %Cu milled powder.

Phase	Composition (at.%)	
	Cu	Sn
Bright (1)	1.94	98.06
Dark (2)	64.7	35.3
Grey (3)	0	100

As shown in Figure 2, the particle shape was initially flaky and large fragments were present, while later stages of the milling process showed finer spherical shaped particles. In HEBM, the plastic deformation, cold welding, and refracturing of metal powders depend upon the mechanical properties of the constituent powder particles [26–28]. In the present investigation, both Cu and Sn are plastic components; therefore, they deform following the plastic-plastic particle system according to Suryanarayana [26]. These plastic–plastic couples flattened to a high surface area structure through a micro-forging process [26]. In due course, the Sn and Cu powder particles overlapped and rewelded to form a lamellar composite structure as shown in (Figure 2a,b).

A shorter diffusion path in the cold-welded lamellar structure and a higher defect ratio accelerated the alloying of Cu and Sn. The solid-state reaction between Cu and Sn led to the formation of Cu_6Sn_5 IMCs (Figure 2c). With prolonged milling times, lamellar composite fragments became work hardened and brittle [26–28]. These brittle particles fractured easily through nucleation and the growth of microcracks in big particles, which resulted in smaller spherical particles (Figure 2d). Agglomeration of these particles may also occur; however, the loose agglomerates were crushed down to fine particles (Figure 2e).

The microhardness of the samples for various milling times is shown in Figure 3. The microhardness of the Sn-0.7Cu alloy increased with milling time, reaching its maximum value at 45 h. The increase in the microhardness value was mainly related to the stored strain energy, as well as a decrease in crystallite size as already discussed. In the observed alloying process, the microhardness showed a linear dependence on the milling time.

**Figure 3.** Vickers microhardness of the Sn-0.7Cu alloy as a function of milling time.

Accordingly, the microhardness can be linearly fitted as [39]

$$HV = U + Vt. \quad (2)$$

Therefore,

$$\ln \frac{L_0}{L_t} = \frac{K}{V} \ln \left[1 + \frac{V}{U} t \right] \quad (3)$$

Here, K , U , and V are constants. t is the milling time, and L represents the thickness of each layer (lamellae) of composite powder. U and V indicate the intercept and slope in Figure 3. $K \approx 134$ is given by Equation (3) for $t = 5$, $L_5 = 44 \mu\text{m}$, and for $t = 25$ h, $L_{25} = 1.34 \mu\text{m}$. With continuous milling of up to 45 h, the lamellar thickness decreased severely, confirming the alloying, which is also supported by SEM results.

The thermal properties of the HEBM-ed Sn-0.7Cu alloy were assessed via DSC experiments, as shown in Figure 4.

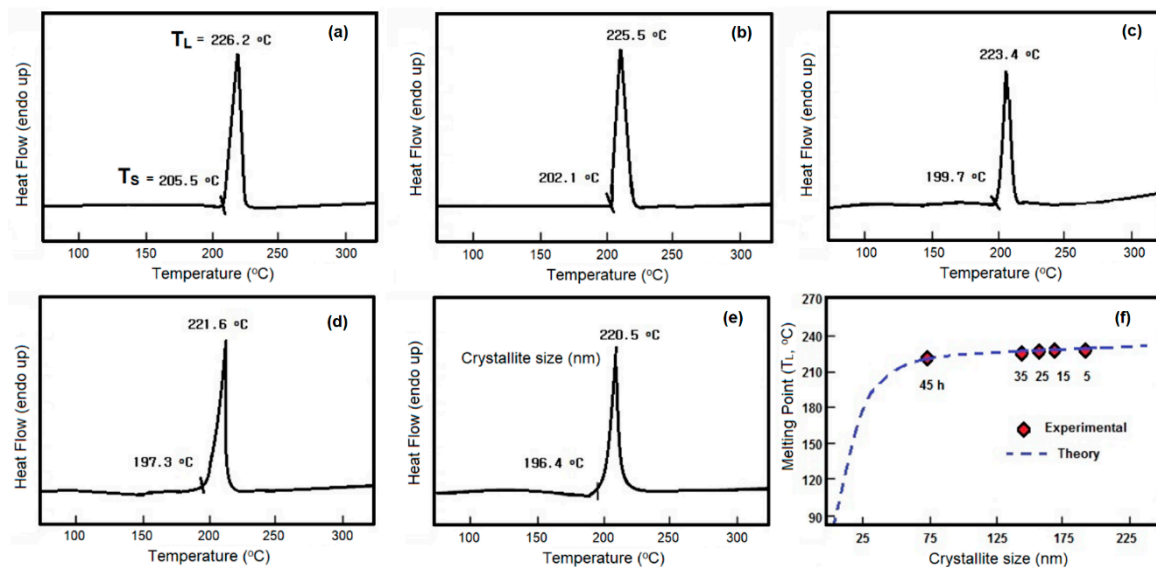


Figure 4. The differential scanning calorimetry (DSC) curve of the Sn-0.7Cu alloy after HEBM for different milling times. (a) 5 h, (b) 15 h, (c) 25 h, (d) 35 h, (e) 45 h, and (f) liquidus of the Sn-0.7Cu alloy as a function of crystallite size.

The solidus temperature (T_S) decreased down to 196.4 °C after milling for 45 h (Figure 4a–e). It is already shown that the milling induced crystal refinement and raised the stored energy, which lowered the Gibbs free energy and created a noted depression in the melting point [26,27]. The various melting temperatures (liquidus (T_L), solidus (T_S), pasty range ($T_L - T_S$)) and enthalpy are shown in Table 4.

Table 4. Thermal characteristics of Sn-0.7 alloy as a function of milling time.

Milling Time (h)	Solidus (T_S) (°C)	Liquidus (T_L) (°C)	Pasty Range ($T_L - T_S$) (°C)	Enthalpy (J/g)
5	205.5	226.2	20.7	57.8
15	202.1	225.5	23.4	57.3
25	199.7	223.4	23.7	55.4
35	197.3	221.6	24.3	53.2
45	196.4	220.5	24.1	52.1

Previous reports have shown that enthalpy changes inversely to the grain size of the powder particles [9]. This means that stored enthalpy rises as milling proceeds for a longer time. The liquidus temperature of the Sn-0.7Cu alloy was 220.5 °C after 45 h of milling, which showed an almost 7 °C depression in the melting point, compared to existing cast Sn-0.7Cu alloys in literatures [1–5]. A depression in the melting point is beneficial, as it results in the lower service temperature and increasingly cost-effective performance of electronic devices.

From Table 4, it is seen that solidus (T_S) and liquidus (T_L) temperatures shifted to a lower temperature as milling time increased. Due to the severe fracturing of the powder particles and the lattice defects induced during HEBM, the stored energy of the powder increased significantly. During heating, the deformation energy lowered the activation energy for grain growth and released the buildup of stresses in the material. A combination of recovery, recrystallization, and grain growth occurred during heating, reducing the overall stored internal energy of the system. Dislocations were eliminated/rearranged during the recovery process, followed by recrystallization and subsequent grain growth [40].

To assess the effect of milling on the melting point of Sn-0.7Cu alloy, we calculated the depression in melting point theoretically as a function of crystallite size using the following model [20,41]:

$$\Delta T = T_{m,bulk} - T_{m,r} = \frac{T_{m,bulk}}{H_{m,bulk} * \rho_s r} \left[\sigma_s - \sigma_l \left(\frac{\rho_s}{\rho_l} \right)^{\frac{2}{3}} \right] \quad (4)$$

where ΔT shows the melting point difference of bulk ($T_{m,bulk} = 227 \text{ }^\circ\text{C}$) and nanocrystalline solid ($T_{m,r} < T_{m,bulk}$), $H_{m,bulk}$ represents the enthalpy of melting of solid material ($\approx 58.6 \text{ J/g}$), ρ_s and ρ_l denote the density of the material in the solid and liquid phases ($\approx 7.29 \text{ g/cm}^3$), σ_s and σ_l denote the surface tensions of the bulk ($\approx 0.584 \text{ J/m}^2$) and liquid phase material ($\approx 0.494 \text{ J/m}^2$), and r is the radius of powder particles. The density and surface tension data were used from [1].

The calculated melting point data were very close to the experimentally observed melting temperatures. It is also noteworthy that the melting point decreased rapidly as soon as the particle size dropped to below $\approx 25 \text{ nm}$ (Figure 4f).

The wetting of the milled powders was calculated by the area spread ratio technique. The milled Sn-0.7Cu powders were reflowed over the metallic Cu substrates at $250 \text{ }^\circ\text{C}$ for 70 s. The reflow profile adopted for the spread ratio measurements is shown in Figure 5.

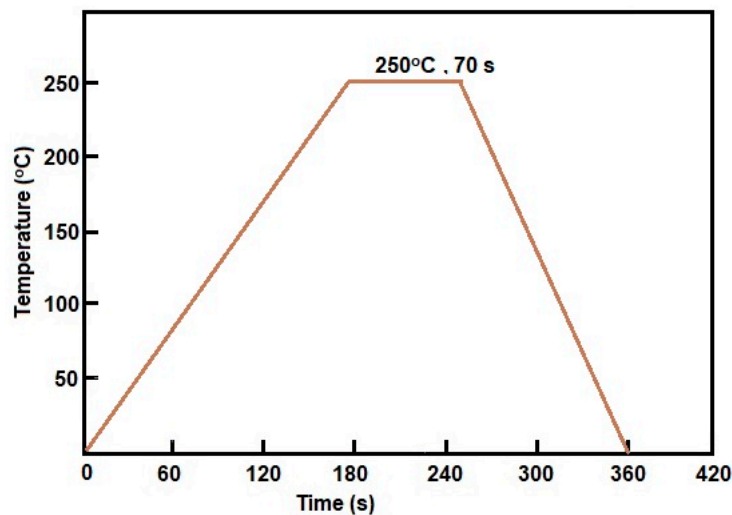


Figure 5. The reflow profile for the measurement of the solderability of the Sn-0.7Cu alloy.

The area spread ratio was calculated by the following relation:

$$\text{Spread ratio (\%)} = \frac{(A_f - A_i)}{A_i}, \quad (5)$$

Here, $A_f - A_i$ is the difference between the final and initial spread areas. The spread ratio of Sn-0.7Cu alloy as a function of milling time is shown in Table 5. The results indicate that the area spread ratio improved continuously with milling time.

Table 5. The solderability of the Sn-0.7 wt. % Cu powder after various milling times.

Milling Time (h)	Spread Ratio (%)	Error (%)
5	63	±2
15	72	±4
25	75	±5
35	80	±6
45	84	±7

It should be noted that the nanostructuring of the powder particles assisted in lowering the interfacial tension at the contact surfaces [42]. The nanostructured powder particles had higher surface energy than the unmilled powder. Therefore, the spread ratio improved [43,44]. The area spread ratio was 63% for 5 h milled powder, and increased rapidly to 80% for 35 h milled powder due to the rapid nanostructuring of powder particles. The maximum spread ratio ($\approx 84\%$) was achieved at a milling time of 45 h.

Spreading demonstrates the ability of the liquid metal to keep contact with the solid surface. When two contact surfaces are brought together in intimate contact, the intermolecular forces of attraction become operative. According to Thomas Young, these forces are related to the surface energy of the solid, liquid, and vapor interfaces and wetting angle given by

$$\gamma_{sv} - \gamma_{sl} = \gamma_{lv} \cos\theta \quad (6)$$

Here, γ_{sv} and γ_{lv} denote the interfacial energy of the condensed phase and γ_{sl} denotes the interfacial energy of the solid-liquid interface. Therefore, a higher spreading of the liquid indicates a smaller value of wetting angle θ .

The possible reason for the smaller wetting angle of the milled powder is that the nanostructured powder particles had a positive impact on the wettability. With an increase in milling time, the powder particles were broken down into high-surface-energy nanoparticles. The milled Sn-0.7Cu powder particles were more likely to wet the interface between the liquid Sn-0.7Cu and Cu substrate, thus lowering the interfacial surface energy between the liquid Sn-0.7Cu and Cu substrate, resulting in a smaller wetting angle and improved spreading. Therefore, the spreading of the powder increased with milling time.

For high-end electronic devices, the wettability factor is most important for soldering. A good wetting ensures the proper bonding of the solder alloy to the metallic substrate. This result depicted that the use of HEBM was advantageous to enhance the solderability of the Sn-0.7Cu alloy on copper conductors. Similarly, the thermal and microstructural properties were also improved via the HEBM approach, for potential application in Pb-free electronic devices.

4. Conclusions and Future Research Directions

1. Eutectic Sn-0.7Cu alloy was successfully produced by HEBM for 45 h. The XRD results showed that the crystallite size of the Sn-0.7Cu alloy was decreased down to 76 nm after 45 h of HEBM.
2. Microhardness of the HEBM-ed Sn-0.7Cu alloy increased continuously with milling time. The maximum hardness (≈ 63 HV) was obtained for 45 milled powder.
3. It was shown that HEBM up to 45 h decreased the solidus and liquidus melting temperatures down to 196.4 °C and 220.5 °C, respectively.
4. There was a considerable depression of ~ 7 °C in the melting point of 45 h ball milled Sn-0.7Cu alloy. The spreadability of HEBM-ed Sn-0.7Cu powder improved significantly, to 84%, after 45 h of HEBM.
5. Although interesting observations have been made in this work, much work remains to study the application of the Sn-0.7Cu alloy in electronic packaging. The future work directions include the application of the Sn-0.7Cu nanopowder for the reflow soldering on Cu and electroless nickel immersion gold (ENIG) substrates in chip-scale devices.

6. The results can also be applied to study the thermomechanical fatigue and fretting-wear properties of the reflowed solders. The study of thermal stability of the developed solders at higher reflow temperatures also requires further attention.
7. Various solder alloys have already been tested for high-temperature thermal shock reliability; nevertheless, most of the Sn-Cu alloys need further research to obtain a better understanding of their performance.

Author Contributions: Conceptualization, B.A.; formal analysis, A.S. and B.A.; funding acquisition, H.S.; investigation, A.S., M.C.O., M.J.C.; methodology, A.S.; resources, H.S.; B.A.; supervision, B.A.; validation, B.A.; writing—original draft, A.S.; writing—review and editing, H.S.; B.A. All authors have read and agreed to the published version of the manuscript.

Funding: This work was supported by the Ajou University Research Fund.

Acknowledgments: This work was supported by the Ajou University Research Fund.

Conflicts of Interest: The authors declare no conflicts of interest.

References

1. Abtew, M.; Selvaduray, G. Lead-free solders in microelectronics. *Mater. Sci. Eng. R* **2000**, *27*, 95–141. [[CrossRef](#)]
2. Zeng, K.; Tu, K.N. Six cases of reliability study of Pb-free solder joints in electronic packaging technology. *Mater. Sci. Eng. R* **2002**, *38*, 55–105. [[CrossRef](#)]
3. Cheng, S.; Huang, C.M.; Pecht, M. A review of lead-free solders for electronics application. *Microelectron. Reliab.* **2017**, *75*, 77–95. [[CrossRef](#)]
4. Ma, H.; Suhling, J.C. A review of mechanical properties of lead-free solders for electronic packaging. *J. Mater. Sci.* **2009**, *44*, 1141–1158. [[CrossRef](#)]
5. Suganuma, K. Advances in lead-free electronics soldering. *Curr. Opin. Solid State. Mater.* **2001**, *5*, 55–64. [[CrossRef](#)]
6. Guo, F.J. Composite lead-free electronic solders. *Mater. Sci. Mater. Electron.* **2007**, *18*, 129–145. [[CrossRef](#)]
7. Puttlitz, K.J.; Stalter, K.A. *Handbook of Lead-Free Solder Technology for Microelectronic Assemblies*; Marcel Dekker: New York, NY, USA, 2004.
8. Kim, K.S.; Huh, H.S.; Suganuma, K. Effects of intermetallic compounds on properties of Sn–Ag–Cu lead-free soldered joints. *J. Alloy. Compd.* **2003**, *352*, 226–236. [[CrossRef](#)]
9. Wu, C.M.L.; Yu, D.Q.; Law, C.M.T.; Wang, L. Properties of Pb-free solder alloys with rare earth element additions. *Mater. Sci. Eng. R* **2004**, *44*, 1–44. [[CrossRef](#)]
10. Lee, T.Y.; Choi, W.J.; Tu, K.N.; Jang, J.W.; Kuo, S.M.; Lin, J.K.; Frear, D.R.; Zeng, K.; Kivilahti, J.K. Morphology, kinetics, and thermodynamics of solid state aging of eutectic SnPb and Pb-free solders (SnAg, SnAgCu, and SnCu) on Cu. *J. Mater. Res.* **2002**, *17*, 291–301. [[CrossRef](#)]
11. Ki, Y.S.; Kim, H.I.; Kim, J.M.; Shin, Y.E. Prediction of thermal fatigue life on mBGA solder joint using Sn-3.5Ag, Sn-3.5Ag-0.7Cu, Sn-3.5Ag-3.0In-0.5Bi solder alloys. *JWJ* **2003**, *21*, 92–98.
12. Park, J.H.; Lee, H.Y.; Jhun, J.H.; Cheon, C.S.; Jung, J.P. Characteristics of Sn–1.7Bi–0.7Cu–0.6In lead-free solder. *JWJ* **2008**, *26*, 43–48.
13. Moon, J.W.; Kim, M.I.I.; Jung, J.P. A study on the soldering characteristics of Sn–Ag–Bi–In ball in BGA. *JWJ* **2002**, *20*, 99–103.
14. Kotadia, H.R.; Mokhtari, O.; Clode, M.P.; Green, M.A.; Mannan, S.H. Intermetallic compound growth suppression at high temperature in SAC solders with Zn addition on Cu and Ni–P substrates. *J. Alloys Compd.* **2012**, *511*, 176–188. [[CrossRef](#)]
15. Myung, W.R.; Ko, M.K.; Kim, Y.J. Effects of Ag content on the reliability of LED package component with Sn–Bi–Ag solder. *J. Mater. Sci. Mater. Electron.* **2015**, *26*, 8707–8713. [[CrossRef](#)]
16. Zhang, L.; Sun, L.; Guo, Y.H. Microstructures and properties of Sn58Bi, Sn35Bi0.3Ag, Sn35Bi1.0Ag solder and solder joints. *J. Mater. Sci. Mater. Electron.* **2015**, *26*, 7629–7634. [[CrossRef](#)]
17. Zhao, M.; Zhang, L.; Liu, Z.Q.; Xiong, M.-Y.; Sun, L. Structure and properties of Sn–Cu lead-free solders in electronics packaging. *Sci. Technol. Adv. Mater.* **2019**, *20*, 421–444. [[CrossRef](#)]

18. Nishikawa, H.; Piao, J.Y.; Takemoto, T. Interfacial reaction between Sn-0.7Cu(-Ni) solder and Cu substrate. *J. Electron. Mater.* **2006**, *35*, 1127–1132. [[CrossRef](#)]
19. Kotadia, H.R.; Howes, P.D.; Mannan, S.H. A review: On the development of low melting temperature Pb-free solders. *Microelectron. Reliab.* **2014**, *54*, 1253–1273. [[CrossRef](#)]
20. Buffat, P.; Borel, J.P. Size effect on the melting temperature of gold particles. *Phys. Rev. A* **1976**, *13*, 2287–2298. [[CrossRef](#)]
21. Nanda, K.K. Size-dependent melting of nanoparticles: Hundred years of thermodynamic model. *Pramana* **2009**, *72*, 617–628. [[CrossRef](#)]
22. Letellier, P.; Mayaffre, A.; Turmine, M. Melting point depression of nanosolids: Nonextensive thermodynamics approach. *Phys. Rev. B* **2007**, *76*, 045428. [[CrossRef](#)]
23. Lee, H.Y.; Sharma, A.; Kee, S.H.; Lee, Y.W.; Moon, J.T.; Jung, J.P. Effect of aluminium additions on wettability and intermetallic compound (IMC) growth of lead free Sn (2 wt. % Ag, 5 wt. % Bi) soldered joints. *Electron. Mater. Lett.* **2014**, *10*, 997–1004. [[CrossRef](#)]
24. Shen, J.; Chan, Y.C. Research advances in nano-composite solders. *Microelectron. Reliab.* **2009**, *49*, 223–234. [[CrossRef](#)]
25. Sharma, A.; Das, S.; Das, K. Pulse Electrodeposition of Lead-Free Tin-Based Composites for Microelectronic Packaging. In *Electrodeposition of Composite Materials*; Mohamed, A.M.A., Golden, T.D., Eds.; InTech: Rijeka, Croatia, 2016; pp. 253–274.
26. Suryanarayana, C. Mechanical alloying and milling. *Prog. Mater. Sci.* **2001**, *46*, 1–184. [[CrossRef](#)]
27. Koch, C.C. Synthesis of nanostructured materials by mechanical milling: Problems and opportunities. *Nanostruct. Mater.* **1997**, *9*, 13–22. [[CrossRef](#)]
28. Koch, C.C.; Scattergood, R.O.; Youssef, K.M.; Chan, E.; Zhu, Y.T. Nanostructured materials by mechanical alloying: New results on property enhancement. *J. Mater. Sci.* **2010**, *45*, 4725–4732. [[CrossRef](#)]
29. Huang, M.L.; Wu, C.M.L.; Lai, J.K.L.; Wang, L.; Wang, F.G. Lead free solder alloys Sn-Zn and Sn-Sb prepared by mechanical alloying. *J. Mater. Sci. Mater. Electron.* **2000**, *11*, 57–65.
30. Lai, L.H.; Duh, J.G. Lead-free Sn–Ag and Sn–Ag–Bi solder powders prepared by mechanical alloying. *J. Electron. Mater.* **2003**, *32*, 215–220. [[CrossRef](#)]
31. Nai, S.M.L.; Wei, J.; Gupta, M. Lead free solder reinforced with multiwalled carbon nanotubes. *J. Electron. Mater.* **2006**, *35*, 1518–1522. [[CrossRef](#)]
32. Sharma, A.; Sohn, H.R.; Jung, J.P. Effect of graphene nanoplatelets on wetting, microstructure, and tensile characteristics of Sn-3.0 Ag-0.5 Cu (SAC) alloy. *Metall. Mater. Trans A* **2016**, *47*, 494–503. [[CrossRef](#)]
33. Babaghorbani, P.; Nai, S.M.L.; Gupta, M. Development of lead-free Sn–3.5Ag/SnO₂ nanocomposite solders. *J. Mater. Sci. Mater. Electron.* **2009**, *20*, 571–576. [[CrossRef](#)]
34. Gain, A.K.; Chan, Y.C.; Yung, W.K.C. Microstructure, thermal analysis and hardness of a Sn-Ag-Cu-1 wt. % nano-TiO₂ composite solder on flexible ball grid array substrates. *Microelectron. Reliab.* **2011**, *51*, 975–984. [[CrossRef](#)]
35. Liu, P.; Yao, P.; Liu, J. Effect of SiC nanoparticle additions on microstructure and microhardness of Sn-Ag-Cu solder alloy. *J. Electron. Mater.* **2008**, *37*, 874–879. [[CrossRef](#)]
36. Mote, V.D.; Purushuttom, Y.; Dole, B.N. Williamson-Hall analysis in estimation of lattice strain in nanometer-sized ZnO particles. *J. Theor. Appl. Phys.* **2012**, *6*, 1–8. [[CrossRef](#)]
37. Alijani, F.; Amini, R.; Ghaffari, M.; Alizadeh, M.; Okyay, A.K. Effect of milling time on the structure, micro-hardness, and thermal behavior of amorphous/nanocrystalline TiNiCu shape memory alloys developed by mechanical alloying. *Mater. Des.* **2014**, *55*, 373–380. [[CrossRef](#)]
38. Reddy, B.; Bhattacharya, P.; Singh, B.; Chattopadhyay, K. The effect of ball milling on the melting behavior of Sn–Cu–Ag eutectic alloy. *J. Mater. Sci.* **2009**, *44*, 2257–2263. [[CrossRef](#)]
39. Benjamin, J.S.; Volin, T.E. The mechanism of mechanical alloying. *Metall. Trans. A* **1974**, *5*, 1929–1934. [[CrossRef](#)]
40. Abdoli, H.; Ghanbarib, M.; Baghshahi, S. Thermal stability of nanostructured aluminum powder synthesized by high-energy milling. *Mater. Sci. Eng. A* **2011**, *528*, 6702–6707. [[CrossRef](#)]
41. Olson, E.A.; Efremov, M.Y.; Zhang, M.; Allen, L.H. Size-dependent melting of Bi nanoparticles. *J. Appl. Phys.* **2005**, *97*, 034304. [[CrossRef](#)]
42. Sharma, A.; Roh, M.H.; Jung, D.H.; Jung, J.P. Effect of ZrO₂ nanoparticles on the microstructure of Al-Si-Cu filler for low-temperature Al brazing applications. *Metall. Mater. Trans. A* **2016**, *47*, 510–521. [[CrossRef](#)]

43. Jung, D.H.; Sharma, A.; Jung, J.P. Influence of dual ceramic nanomaterials on the solderability and interfacial reactions between lead-free Sn-Ag-Cu and a Cu conductor. *J. Alloy Compd.* **2018**, *743*, 300–313. [[CrossRef](#)]
44. Ismail, N.; Ismail, R.; Ubaidillah, N.K.A.N.; Jalar, A.; Zain, N.M. Surface roughness and wettability of SAC/CNT lead free solder. *Mater. Sci. Forum* **2016**, *857*, 73–75. [[CrossRef](#)]



© 2020 by the authors. Licensee MDPI, Basel, Switzerland. This article is an open access article distributed under the terms and conditions of the Creative Commons Attribution (CC BY) license (<http://creativecommons.org/licenses/by/4.0/>).